nature synthesis

Article

https://doi.org/10.1038/s44160-026-01086-5

Solid–solid catalysis for sustainable alloy synthesis

Received: 30 October 2025

Accepted: 28 April 2026

Published online: 08 June 2026

Check for updates

Xinren Chen (陈信任)[1], Baptiste Bienvenu[1], Tingting Yang (杨婷婷)[2], Baptiste Gault[1,3], Shaolou Wei (魏绍楼)[1] ✉, Xuyang Zhou (周徐洋)[1,4] ✉ & Dierk Raabe[1] ✉

Metal production causes 10% of global greenhouse gas emissions, with most metals extracted from oxide ores via fossil-based pyrometallurgy, including melting. Solid-state hydrogen-driven redox reduction is not only a sustainable alternative, but can also be used to integrate reduction, in situ alloying of mixed oxides and microstructure design in one single process. Upon co-reduction of a Fe_2O_3–NiO mixture with hydrogen, we report a distinct type of solid–solid catalytic interaction between pre-reduced metal (Ni) and a transient oxide (FeO). This interaction accelerates hydrogen-based reduction by a factor of at least two, highlighting its potential relevance for improving reduction kinetics in hydrogen-based ironmaking and alloy production. Specifically, during hydrogen-driven co-reduction of Fe_2O_3 and NiO, Ni partitioning takes place across metal–oxide interfaces, driven by interface dynamics, during which restructuring continuously regenerates the catalytic sites that promote H_2 spillover. These findings show that hydrogen-based alloy production is not only more sustainable than fossil-based practices, but can leverage kinetic and commercial advantages through solid–solid catalytic effects.

Metals are extracted from minerals, industrial waste and oxidized scrap through three main reduction principles[1]: pyrometallurgy, hydrometallurgy and electrometallurgy. Pyrometallurgy uses high homologous temperatures to smelt-reduce oxidic feedstocks, such as Fe_2O_3 with CO, in blast furnaces, in a process that is responsible globally for ~10% of energy use and ~8% of CO_2 emissions for steel production alone[2]. Hydrometallurgy uses aqueous leaching, purification and recovery at lower temperatures[3], whereas electrometallurgy cathodically reduces metal ions from molten or aqueous ionic phases, as in Al extraction by the Hall–Héroult process or purification through electrorefining.

For millennia, metal-extraction technologies followed economic, scaling and efficiency needs alone. Today, environmental and regulatory constraints challenge these traditional metal-production routes, particularly in steelmaking[4], thereby leading to innovation in approaches that allow direct synthesis[5] and energy-efficient catalytic pathways[6] that are commercially viable. Solid-state direct reduction[7–10] offers such an alternative: it operates at moderate homologous temperatures, is solvent-free, scalable to million-tonnes-per year reactors, and is accessible to various gaseous reductant types, including sustainably produced hydrogen. Reduction kinetics are governed by redox conditions (temperature, pressure and reductants); transport mechanisms (reductants, redox product(s), metal and oxygen); catalysis effects; phase nucleation, growth and transformations; microstructure and damage; and micromechanical stress and strain fields[11]. Taking, for instance, Fe oxide as a model system, the CO- or H_2-based reduction of haematite (Fe_2O_3) to magnetite (Fe_3O_4)[12–14] follows Avrami nucleation and growth

[1]Max Planck Institute for Sustainable Materials, Düsseldorf, Germany. [2]Ernst Ruska-Centre for Microscopy and Spectroscopy with Electrons and Peter Grünberg Institute, Forschungszentrum Jülich, Jülich, Germany. [3]Univ Rouen Normandie, CNRS, INSA Rouen Normandie, Groupe de Physique des Matériaux UMR 6634, Rouen, France. [4]State Key Laboratory for Mechanical Behavior of Materials, Xi'an Jiaotong University, Center for Advancing Materials Performance from the Nanoscale (CAMP-Nano), Xi'an, P. R. China. ✉e-mail: sl.wei@mpi-susmat.de; x.zhou@xjtu.edu.cn; d.raabe@mpi-susmat.de

https://doi.org/10.1038/s44160-026-01086-5

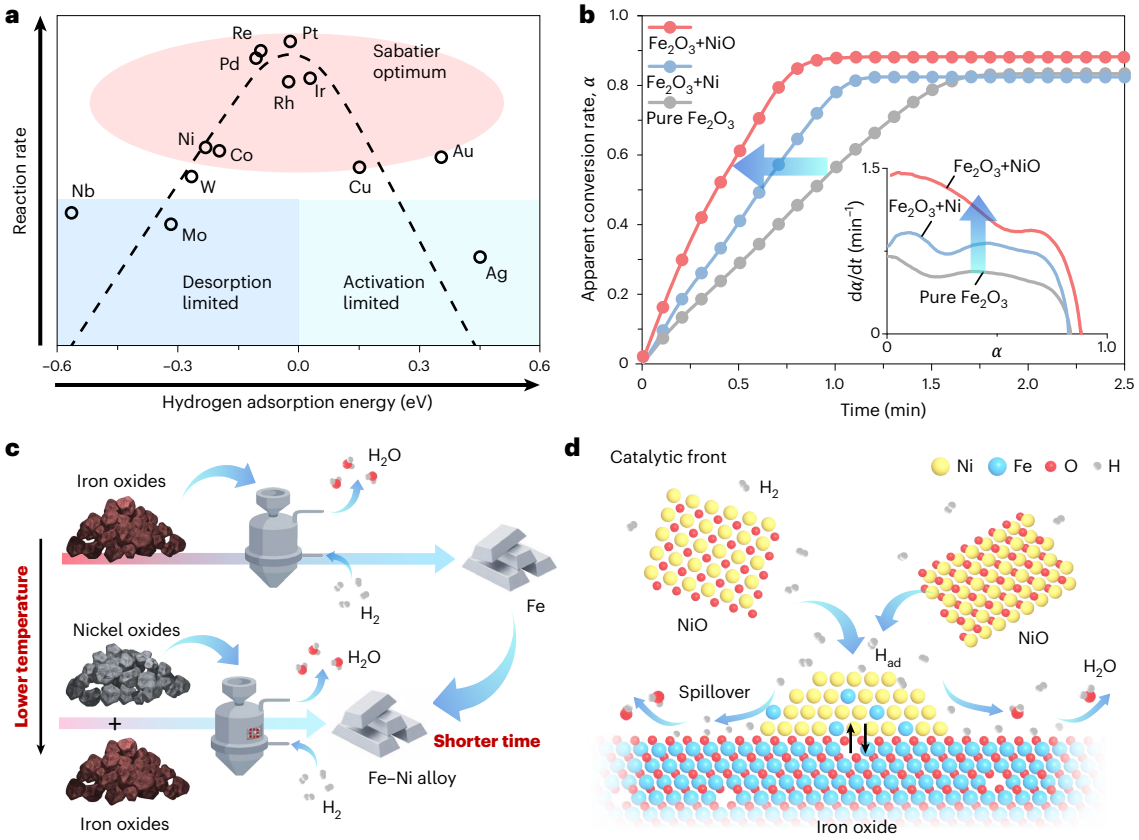

Fig. 1 | Catalysing hydrogen-based iron-oxide reduction via Sabatier-optimized co-reduction. a, Volcano plot of relative reaction rate versus hydrogen adsorption energy, compiled from the literature[21,22]. **b**, Isothermal reduction of Fe_2O_3, Fe_2O_3 + Ni (Fe-36Ni wt.% for the metallic element stoichiometry) and Fe_2O_3 + NiO (targeting the same Fe-36Ni wt.% for metallic species) mixed powders (50 mg) at 700 °C under a 10 l h^{-1} H_2 flow rate. Inset: first-order derivative ($d\alpha/dt$) as a function of conversion, indicating the change in reaction rate. **c**, Schematic comparison of two different direct-reduction pathways. Top: non-catalysed version in which H_2 reduction separately produces Fe (from Fe_2O_3) before subsequent alloy production can be done. Bottom: the same process, but with co-reduction of a stoichiometric Fe_2O_3–NiO mixture, which forms a catalytic metal–oxide front and yields an Fe–Ni alloy in a shorter time. **d**, Schematic illustration of the fast reduction mechanism, where reduced Ni (from NiO) creates a H_2 spillover front that accelerates iron-oxide reduction and enables rapid alloy formation. H_{ad}, surface adhered hydrogen.

kinetics[15]. The subsequent magnetite-wüstite ($Fe_{1-x}O$, where x is the Fe deficiency) transformation is partly topotactic. This means that both phases share an O^{2-} face-centred cubic (fcc) lattice, but it also involves cation rearrangement and non-ideal stoichiometry. $Fe_{1-x}O$ reduction proceeds via nucleation and growth or disproportionation reaction ($Fe_{1-x}O \rightarrow Fe_3O_4 + Fe$), with associated volumetric changes and stresses complicating the final $Fe_{1-x}O \rightarrow Fe$ step[11,16]. The final transition to body-centred cubic (bcc) Fe is diffusion-controlled[15], and the combined effects of mass loss, volumetric shrinkage, phase changes and charge redistribution[5,17] qualify solid-state reduction as a highly complex open-system mechano-chemical process. Considering the scale of global metal production and the long-standing nature of conventional ironmaking and alloying practices, understanding these mechanisms and their interplay is essential for guiding the development of more sustainable and cost-efficient reduction processes.

In this Article, building on our previous demonstration of one-step synthesis of sustainable bulk alloys from oxides[5], we report an apparently distinct phenomenon in that context, namely, a solid–solid catalytic mechanism that facilitates metal extraction from oxides. It works by adding to a gas–solid reduction process of a transition-metal oxide (here Fe_2O_3) a second catalytically acting metal (here Ni) or its reducible transition-metal-oxide precursor (here NiO), which can leverage a sequence of reactive transport microevents that accelerate metal-oxide reduction, as evidenced in the following.

Results and discussion

Solid–solid catalysis

Conventional catalyst selection for hydrogen-based gas–solid direct-reduction processes is guided by a volcano diagram of the hydrogen adsorption energies[18–22] (Fig. 1a). According to the Sabatier principle[23], activity peaks at intermediate binding strength. This sort of mechanistic screening highlights Ni, Co, W and Cu as promising catalyst candidates for hydrogen-based Fe_2O_3 reduction. Noble metals, though active, are less economical. Among these candidates, Ni (refs. 5,24,25) is especially attractive, as it is not only widely used across a broad range of commercial steels (Supplementary Fig. 1), but also offers an attractive combination of high catalytic activity for hydrogen dissociation and excellent thermodynamic and metallurgical compatibility with Fe. These features enable efficient hydrogen-based reduction while avoiding detrimental phase separation or the formation of brittle intermetallic compounds[5]. In contrast, W exhibits sluggish diffusion kinetics that hinder homogenization during reduction, Cu has negligible solid solubility in Fe and tends to develop detrimental segregation during thermo–mechanical processing, and Co does not provide a clear advantage over Ni in stabilizing the reduced metallic phase or enhancing reduction kinetics.

As shown in Fig. 1b, the addition of metallic Ni (particle size ~300 nm) noticeably shortens the Fe_2O_3 reduction saturation time at 700 °C—by a factor of 1.6. However, the use of pure metallic catalysts

necessitates carbon-intensive processes for metal extraction[10], thereby increasing both environmental and financial burdens. To overcome this, we propose a co-reduction strategy that directly uses metal oxides or refined ores. Using bunsenite (NiO; particle size ~15 µm) as an example, co-reduction of the two oxides exhibits an even more pronounced catalytic effect, reducing the time-to-saturation state by a factor of 2 at 700 °C. As seen from the inset in Fig. 1b, the reaction rate remains consistently higher with NiO added rather than with metallic Ni addition or standalone Fe_2O_3. To deconvolute the apparent Fe_2O_3 conversion rate contribution due to NiO reduction, in Supplementary Fig. 2 we provide the kinetic quantification after subtracting the NiO effect. Furthermore, the addition of Ni or NiO lowers the onset temperature of Fe_2O_3 reduction by at least ~100 °C (Supplementary Fig. 3) when the process takes place in a continuous heating operation manner, mimicking industrial direct-reduction practices. Although demonstrated here on a 50-mg laboratory-scale sample, the synergistic reduction mechanisms identified here at the near-atomic scale are expected to persist at larger scales, providing a catalytic pathway to decrease reduction temperatures, shorten processing times, lower energy consumption, and enable sustainable one-step master alloy production (Fig. 1c).

We ascribe the catalytic effect at this reduction temperature to the H_2 spillover mechanism at metal–oxide interfaces[26–29]. NiO is rapidly reduced by H_2 (ref. 30), forming nanocrystalline, highly porous metallic Ni (Supplementary Fig. 4). The resulting porous Ni establishes contact with adjacent Fe oxides, creating interfacial regions where the reduced Ni catalyses H_2 dissociation and promotes hydrogen spillover[28,31–34], as shown in Fig. 1d.

The higher conversion rate observed in the Fe_2O_3–NiO mixture compared with the Fe_2O_3–Ni mixture arises from the in situ generation of finely dispersed, porous Ni during NiO reduction (Supplementary Fig. 4d–i), which maximizes both the Ni–FeO interfacial area and the associated catalytic activity. In contrast, pre-existing metallic Ni largely retains its initial morphology but becomes partially encapsulated by reduced Fe during reduction, limiting gas transport and resulting in less active interfacial junctions, as evidenced by the comparison shown in Supplementary Fig. 5.

Kinetic enhancement mechanisms

We conducted an in situ synchrotron X-ray diffraction (SXRD) experiment to study the kinetics of hydrogen-based co-reduction of an Fe–Ni oxide model system with a hydrogen flow rate of ~0.6 l h^{-1}. Figure 2a–c shows that the main reaction cascade starts at 700 °C (0 s), a stage at which the system contains Fe_3O_4 (converted from Fe_2O_3 during heating), NiO and some metallic fcc Ni formed from the partial reduction of NiO during heating. After 330 s at 700 °C, NiO has been fully converted to metallic fcc Ni. This initial step is considered the 'fast stage' of the reduction process[5]. Beyond this point, the main rate-limiting step commences, in which $Fe_{1-x}O$ gradually starts converting into metallic Fe. The in situ SXRD data focus on the kinetics and structural evolution during this slow, diffusion-controlled reduction stage. In hydrogen-based reduction, the transformations $Fe_2O_3 \rightarrow Fe_3O_4$ and $Fe_3O_4 \rightarrow Fe_{1-x}O$ proceed rapidly[7]. The rate-limiting step is $Fe_{1-x}O \rightarrow$ bcc Fe, which is hindered by incomplete H_2O removal[35,36] and the high nucleation barrier of bcc Fe[9,16,37–39].

From 0 s to 1,630 s under an isothermal condition at 700 °C, the SXRD data show progressive intensity decrease of the Fe_3O_4 and $Fe_{1-x}O$ peaks (Fig. 2a), signifying their reduction processes. During the reduction, no bcc phase emerges (Fig. 2b). Instead, a significant lattice-parameter shift in the metallic fcc Ni phase (Fig. 2c) indicates Fe–Ni alloy formation through partitioning and diffusion of metallic Fe atoms into the fcc Ni lattice. As illustrated schematically in Fig. 1d, Ni nanoparticles formed on the Fe-oxide surface act as sinks for Fe atoms released during Fe-oxide reduction, leading to concurrent Fe–Ni alloy formation rather than the well-established mechanism of post-reduction solid-state interdiffusion. After 1,630 s, most of the reduction and alloying processes have completed. SXRD patterns of bulk samples after holding at 700 °C for a further 1 h (Fig. 2d) confirm that, in the presence of NiO, the fcc phase is formed without the bcc phase (which otherwise remains the only product in the case of pure Fe_2O_3 reduction). Compared with the pure metallic-state interdiffusion reference (cold pressed bulk Fe ~400-nm and Ni ~300-nm powders), which shows clear bcc peaks after the same heat treatment, the Fe_2O_3 + NiO system exhibits a markedly accelerated alloying process during the reduction.

At 730 s, high-angle annular dark-field scanning transmission electron microscopy (HAADF-STEM) imaging reveals the interface between the fcc (Fe, Ni) phase and residual $Fe_{1-x}O$ (Fig. 2e and Supplementary Fig. 6). The corresponding energy-dispersive X-ray spectroscopy (EDS) elemental maps of Fe, Ni and O (Fig. 2f–h) show Fe enrichment at the interface between the fcc Fe–Ni phase and $Fe_{1-x}O$, as well as along the grain boundary between two fcc grains. Upon phase-indexing the four-dimensional STEM (4D-STEM) data, no additional fcc phase formation was detected during this period (Supplementary Fig. 7). At 1,630 s, the EDS map (Supplementary Fig. 8) shows a uniform Fe–Ni distribution with no detectable oxides, and confirms that the initially Ni-rich phase has transformed into the designed Fe–Ni invar alloy.

This accelerated process is illustrated in Fig. 2i, where the mixture of the fcc Ni-rich phase and $Fe_{1-x}O$ directly reduces to an fcc Fe–Ni alloy without formation of any intermediate bcc Fe phase. This means that the first formed Ni metal acts as a direct metallothermic reductant, extracting Fe out of its oxide state. Notably, when compared to the classical interdiffusion process between Fe and Ni, as shown in Fig. 2j,k, alloy formation is significantly accelerated. Based on thermophysical data from the TCFE9 and MOBFE4 databases (Thermo-Calc Software), tracer diffusivity calculations suggest that, under equilibrium conditions at 700 °C for 1,200 s, Fe and Ni should each diffuse only ~10 nm in the Fe–Ni alloy (Fig. 2i), a value far below the critical length scale required for the formation of a local portion of homogeneous Fe–Ni alloy. Interdiffusion simulations further confirm that achieving complete homogenization in a system of comparable dimensions would typically require timescales exceeding five days (120 h) at this temperature (Fig. 2j). In contrast, the in situ SXRD results reveal that alloying in the current distinct reaction pathway is completed within only 30 min, implying that the presence of NiO precursors significantly enhances Fe–Ni interdiffusion and alloy homogenization beyond predictions from classical bulk diffusion models.

These results indicate that alloying occurs concurrently with the reduction process rather than through conventional post-reduction interdiffusion. Under the present catalytic reduction conditions, multiple factors are expected to assist direct alloying, including the formation of porosity, cation diffusion[40] through non-stoichiometric $Fe_{1-x}O$, as well as the development of an ultra-fine-grained microstructure, which collectively introduce a high density of grain boundaries and associated fast diffusion pathways[41]. In addition, the presence of a hydrogen atmosphere is likely to increase the vacancy concentration[42] and lower point-defect migration barriers[43]. Altogether, these effects can substantially enhance the mobility of Fe and Ni, thereby promoting defect- and interface-assisted diffusion beyond equilibrium bulk lattice diffusion, as further discussed in Supplementary Note 1.

Structure and chemistry of the metal–oxide interfaces

To more precisely characterize the chemical composition near the metal–oxide interfaces and thus elucidate the reaction mechanism at the interface between metallic fcc grains and $Fe_{1-x}O$, an atom probe tomography (APT) specimen containing such interfaces was prepared, as shown in Fig. 3a. The $Fe_{1-x}O$ phase was identified by 4D-STEM performed on the APT specimen, as highlighted through virtual dark-field imaging (Fig. 3a, inset) of the corresponding diffraction spots (Supplementary Fig. 9). The orientation map reveals the presence of five distinct metallic fcc grains (denoted γ1 to γ5 in Fig. 3b) and the $Fe_{1-x}O$ phase, each with different crystallographic orientations. This

https://doi.org/10.1038/s44160-026-01086-5

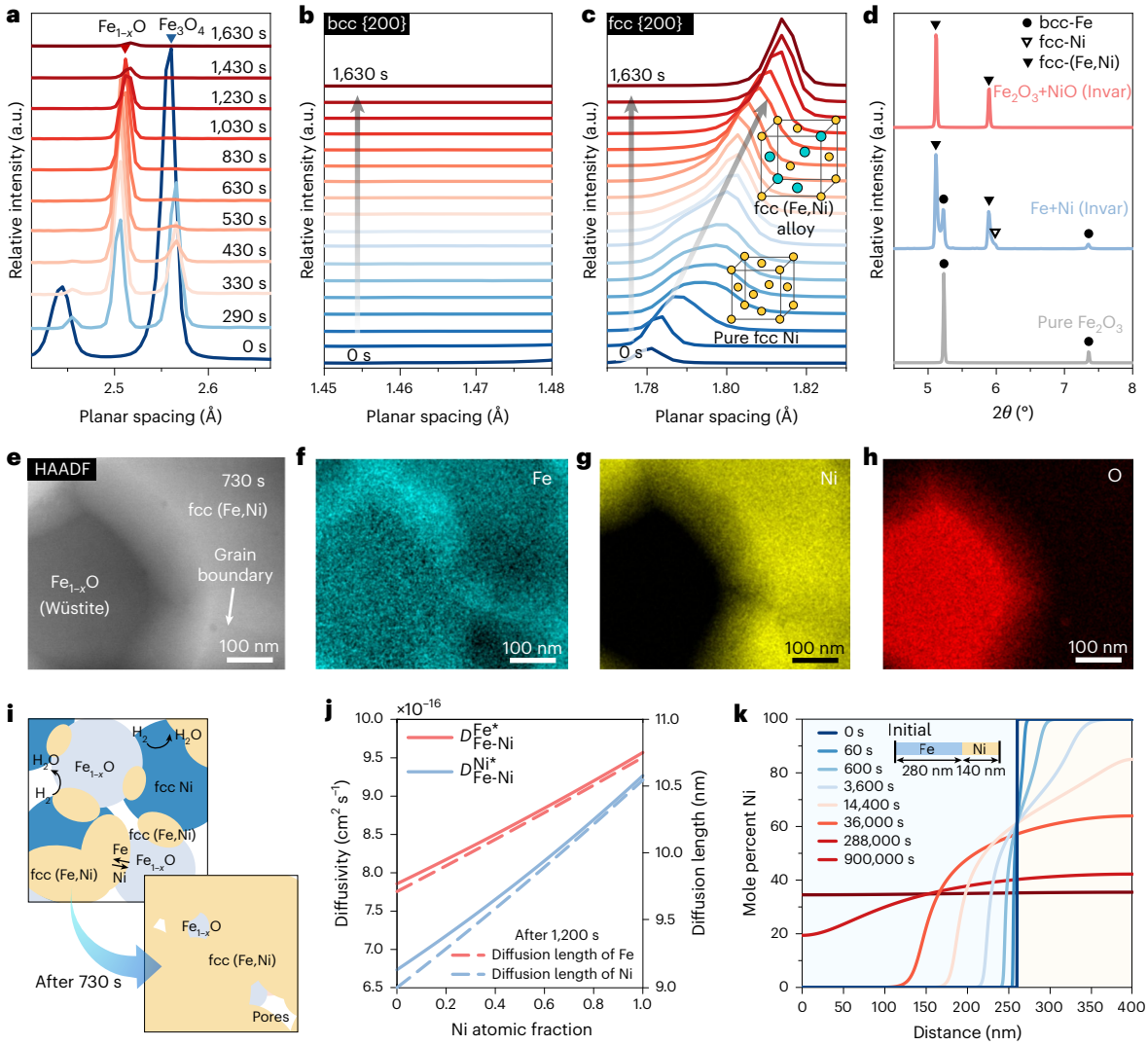

Fig. 2 | Time-resolved characterization of hydrogen-based reduction and alloying. a, In situ SXRD patterns during hydrogen reduction of Fe_2O_3 + NiO (Fe–36Ni wt.%) at 700 °C with a H_2 flow rate of ~0.6 l h^{-1}, showing full conversion of Fe_2O_3 to Fe_3O_4 after reaching 700 °C, followed by rapid disappearance of the Fe_3O_4 phase and the persistence and gradual reduction of $Fe_{1-x}O$. Data reproduced from ref. 5. **b**, Zoomed-in SXRD patterns showing no emergence of the bcc metal {200} peak. **c**, Zoomed-in SXRD patterns showing the evolution of the fcc metal {200} peak. **d**, SXRD patterns of the reduction of bulk samples after holding at 700 °C for 1 h, comparing pure Fe_2O_3, Fe_2O_3 + NiO (Fe–36Ni wt.%) and an interdiffusion reference of Fe + Ni (Fe–36Ni wt.%). **e**, HAADF-STEM image at 730 s. **f**–**h**, Corresponding EDS maps of Fe (**f**), Ni (**g**) and O (**h**). **i**, Schematic of the reaction pathway showing the interface evolution between $Fe_{1-x}O$ and the earlier-reduced Ni at 730 s during hydrogen-based reduction. **j**, Calculated tracer diffusivities (D) of Fe and Ni in fcc Fe-36Ni wt.% alloy at 700 °C as a function of Ni content (left axis), with the corresponding diffusion lengths after 1,200 s (right axis). **k**, Simulated interdiffusion profiles of Ni concentration across a Fe/Ni interface at different times, based on thermodynamic and mobility databases (TCFE9 and MOBFE4), showing sluggish alloying kinetics toward the final Fe–Ni Invar composition.

configuration allows for the analysis of multiple $Fe_{1-x}O$–fcc interfaces within a single sample. Due to the spatial overlap between the $Fe_{1-x}O$ and fcc phases, virtual dark-field images were used to enhance the contrast and clearly delineate their morphology and distribution, as presented in Fig. 3b and Supplementary Fig. 9.

To study the same region at the highest chemical sensitivity, correlative APT results are presented in Fig. 3c, where iso-surfaces in the concentration of Ni (37.0 at.%), Fe (58.0 at.%) and O (30.0 at.%) delineate the grain structures, enabling direct spatial comparison with the 4D-STEM data in Fig. 3b. To investigate elemental distributions at the reduction and alloying fronts, two distinct locations were analysed: one at the interface between the sintering neck (site 1) and $Fe_{1-x}O$, and another at the boundary between a metallic fcc grain (γ3) and $Fe_{1-x}O$ (site 2). At site 1, as shown in Fig. 3d, an Fe-enriched region appears on the metal side adjacent to the metal–oxide interface. This observation suggests that Ni atoms diffusing from the surfaces of Ni precursor grains combine with the reduced Fe, promoting the growth of a metallic fcc (Fe, Ni) phase, instead of forming bcc Fe. In contrast, at the fcc–γ3/$Fe_{1-x}O$ interface (site 2), partitioning between Fe and Ni is observed (Fig. 3e). Interestingly, an ~7 at.% Ni enrichment is detected on the $Fe_{1-x}O$ side of the interface (Fig. 3f). It should be noted that, due to preferential oxygen loss during APT analysis, the measured O content deviates from the ideal $Fe_{1-x}O$ stoichiometry (Supplementary Fig. 10). For wüstite, the apparent O concentration is typically around 40 at.%, as reported in the literature[44].

Figure 3g presents two reaction-driven alloying mechanisms that are likely responsible for the formation of the fcc (Fe, Ni) phase. In mechanism 1 (site 1), Ni and Fe from adjacent fcc grains (for example, γ2 and γ3) migrate via surface and grain boundary diffusion, forming a localized 'sintering neck', and the outward migration and reduction of Fe^{2+} ions from $Fe_{1-x}O$ and inward diffusion of Ni result in the formation of an Fe-enriched metallic fcc alloy at the neck interface. This process is driven by redox reactions and the minimization of surface energy. In

https://doi.org/10.1038/s44160-026-01086-5

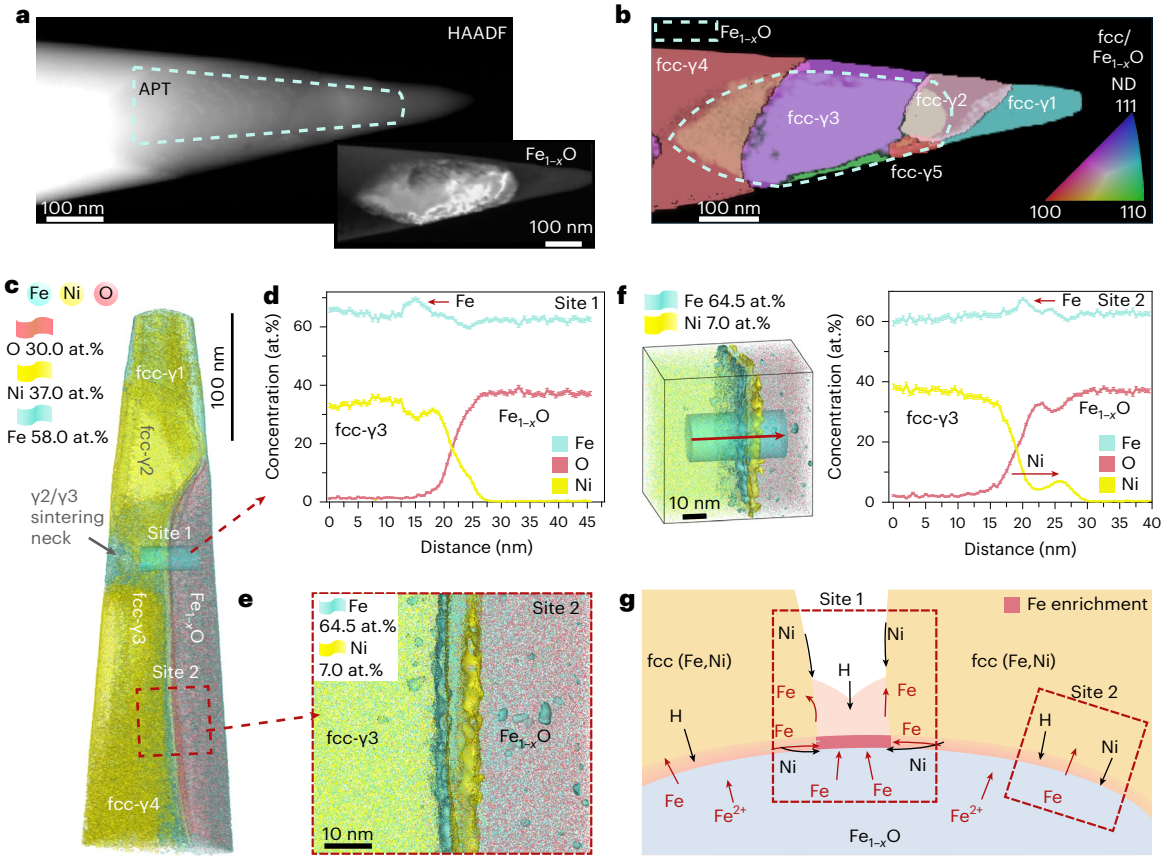

Fig. 3 | Nanoscale reaction interfaces during hydrogen-based reduction. **a**, HAADF-STEM image of a needle-shaped APT specimen extracted from the reaction interface between fcc (Fe, Ni) grains and $Fe_{1-x}O$. Inset: 4D-STEM virtual dark-field image of embedded $Fe_{1-x}O$ (Supplementary Fig. 9). **b**, Correlative 4D-STEM grain orientation map of the same specimen, showing five fcc grains (γ1–γ5) adjacent to $Fe_{1-x}O$, indexed along the normal direction (ND). **c**, APT 3D reconstruction showing the spatial distributions of Fe, Ni and O across fcc grains (γ2–γ4) and neighbouring $Fe_{1-x}O$ regions. **d**, One-dimensional (1D) atomic concentration profile across the fcc–$Fe_{1-x}O$ interface (site 1) at the sintering neck, deliberately selected away from major crystallographic poles (Supplementary Fig. 12). **e**,**f**, Local composition maps at site 2 (**e**) and 1D profiles (**f**) across the fcc γ3/$Fe_{1-x}O$ interface, acquired from regions not intersecting major crystallographic poles, thereby minimizing pole-related evaporation artefacts (Supplementary Fig. 12). **g**, Schematic of two proposed reduction mechanisms occurring at sites 1 and 2, respectively.

mechanism 2 (site 2), Ni diffuses directly along the $Fe_{1-x}O$ interface into regions where Fe is being reduced by hydrogen, enabling the growth of a continuous fcc (Fe, Ni) phase (Supplementary Fig. 11) without a sintering neck. Although there is a difference in diffusion micro-mechanisms, both phenomena emphasize the coupling of elemental diffusion with hydrogen-induced reduction to enable the observed transformations and solid solution states.

Spillover-driven local interfacial redox partitioning cycle

Metal–oxide interfaces play a critical role in redox catalysis[45–47], where oxygen vacancies facilitate charge transfer dynamics[48]. Incorporation of Ni enhances H_2 dissociation and spillover[28,31,32], sustaining catalytic activity.

During hydrogen reduction of $Fe_{1-x}O$ (Fig. 4a,b), Ni effectively splits the H_2 into adsorbed H atoms on the metal surface or interfaces[49], which migrate to the adjacent oxide (H_2 spillover) and facilitate oxygen removal[50]. Lattice oxygen (O^{2-}) reacts with spillover H to form H_2O, creating oxygen vacancies ($V_O^{\bullet\bullet}$, Kröger–Vink notation[51]). Charge neutrality is maintained by creating cation vacancies (V''_{Fe})[52]. These vacancies distort local coordination, attracting nearby Fe into tetrahedral sites that temporarily impede reduction. As H_2 is consumed and the partial pressure of water vapor P_{H_2O} rises, both Fe and Ni are reoxidized[35] (Fig. 4c). During the initial stage of reoxidation, an $(Fe,Ni)_{1-x}O$ layer forms between the metallic Ni–Fe alloy and the adjacent $Fe_{1-x}O$ phase, as shown in Fig. 4d. This double-layer structure has also been reported in naturally formed oxidation layers[53,54]. However, in the present case, $Fe_{1-x}O$ is already present before reoxidation. The thickness of the $(Fe,Ni)_{1-x}O$ layer is controlled by the local value of P_{H_2O} and the rate of reoxidation at the interface.

In the subsequent step, as P_{H_2O} decreases due to interfacial diffusion and renewed H_2 supply, Ni^{2+} is reduced back to metallic Ni, regenerating active Ni–$Fe_{1-x}O$ interfaces. Repeated redox cycles leave behind a transient Ni-enriched layer within the $Fe_{1-x}O$ (Fig. 4d), coupling rapid H_2 activation on Ni with fast co-reduction of Ni and Fe to drive fcc alloy growth[33], bypassing the usually expected conventional bcc nucleation pathway.

It should also be noted that in regions near the reaction interface, as shown in Fig. 4e, Fe^{2+} and Ni^{2+} diffuse via the same population of cation vacancies in non-stoichiometric $(Fe,Ni)_{1-x}O$, and the ratio of their effective diffusivities is governed by their vacancy exchange frequencies. Literature data indicate that the mobility of Fe^{2+} in wüstite-type oxides exceeds that of Ni^{2+} by a factor of ~3–10 at comparable temperatures[40] (Supplementary Note 1). This kinetic difference gives rise to the detention of Ni beneath the oxide surface during multiple cycles.

The formation of Ni^{2+} inclusions during reoxidation is a redox-related partitioning step within $Fe_{1-x}O$ that might be driven by thermodynamic partitioning at the metal–oxide interface. To quantify this effect, we performed density functional theory (DFT) calculations (Methods) and defined the partitioning enthalpy H_p as the energy difference between the pristine and the co-substituted systems, respectively

https://doi.org/10.1038/s44160-026-01086-5

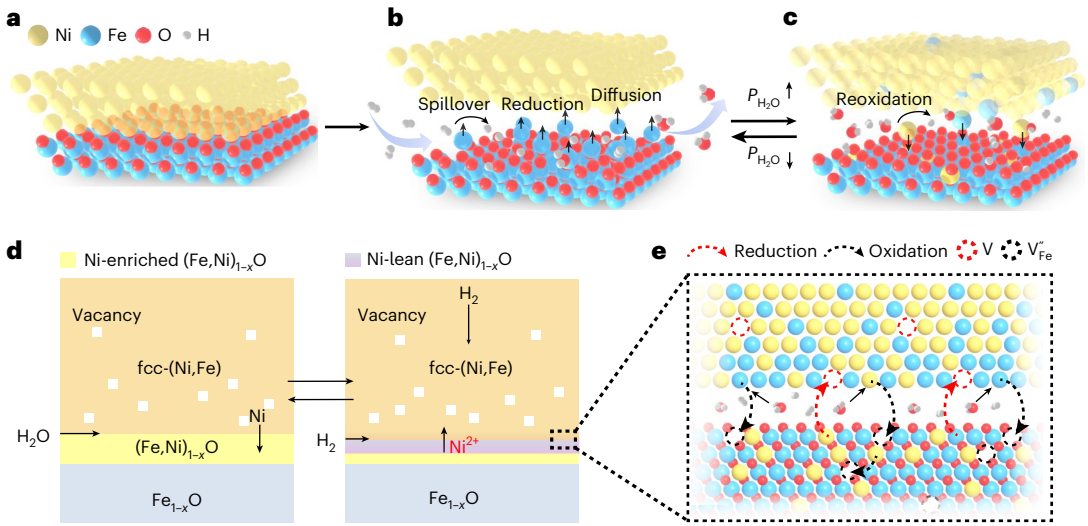

Fig. 4 | Schematic of the hydrogen spillover-driven redox cycle at the metal–oxide interface. a, Early-reduced Ni contacts $Fe_{1-x}O$. **b**, H_2 molecules dissociate on Ni and spill over to $Fe_{1-x}O$, promoting interfacial reduction. **c**, The interfacial region undergoes reoxidation. **d**, Schematic illustration of the dynamic evolution of the oxide–metal interface during repeated reduction–reoxidation cycles. **e**, Zoom-in of the reaction front: coupled reduction/oxidation loops generate/annihilate point defects, such as V (vacancy in the fcc lattice) and V''_{Fe} (cation vacancy), continually regenerating active sites and sustaining accelerated $Fe_{1-x}O$ reduction and alloying with Ni.

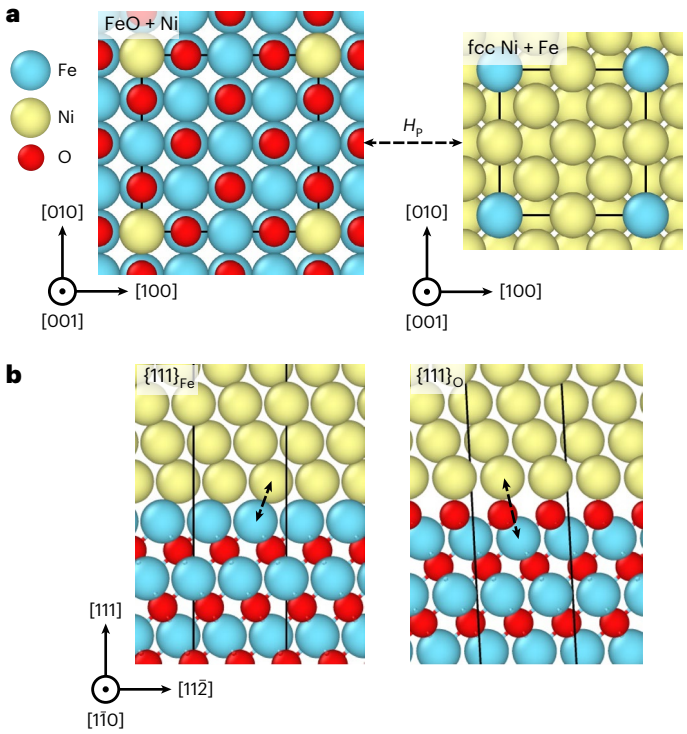

Fig. 5 | Solid-state partitioning between metallic fcc Ni and stoichiometric FeO based on DFT calculations. a, Structural models used in the DFT calculations, representing the bulk partitioning tendency between fcc Ni and stoichiometric FeO. **b**, The two Fe- and O-terminated configurations of the $\{111\}_{Ni}/\{111\}_{FeO}$ interface considered in the DFT calculations. The two dashed arrows indicate the Fe and Ni atoms that are swapped for evaluating the partitioning enthalpy H_P at the interface. Thick black lines show the limit of the periodic simulation cells used in the simulations.

(Fig. 5a). For bulk metallic fcc Ni and ideally stoichiometric FeO, DFT calculations based on the metaGGA-r^{2}SCAN x-c functional predict an H_P of −0.26 eV, indicating a thermodynamic driving force for solid-state partitioning and direct reduction of the oxide through metallic Ni. Supplementary Table 1 shows that the Ni–FeO pair exhibits the strongest driving force among all possible Ni/Fe oxide combinations. The consistent results for the non-stoichiometric model are presented in Supplementary Note 2 and Supplementary Fig. 13.

For this analysis we have considered a prototypical coherent interface model with a $\{111\}_{FCC}$ to $\{111\}_{FeO}$ orientation relationship, minimizing the lattice mismatch between the two materials to ~2%, depending on the x-c functional used in the DFT calculations. This interface has two different configurations, depending on whether an Fe- or O-terminated {111} layer of stoichiometric FeO is in contact with the fcc Ni (Fig. 5b). DFT simulations predict H_P = +0.25 eV for the Fe-terminated interface (partitioning unfavourable) and −0.21 eV for the O-terminated interface (partitioning favourable), consistent with bulk behaviour. Thus, intermixing can proceed as the interface migrates during reduction, supporting our experimental observations of Ni^{2+} partitioning and enhanced reaction kinetics.

Across redox cycles, Fe and Ni re-enter $Fe_{1-x}O$ cation sites, generating vacancies at the fcc (Ni,Fe) surface. These vacancies may readily cluster into the forms of nano-voids at 700 °C, but can also be refilled by reduced Fe in subsequent cycles, leveraging enhanced diffusion and promoting alloying. This mechanism probably accounts for the diffusion enhancement that underpins the accelerated alloying process described above.

We note that a simple thermodynamic descriptor—the value of H_P—allows for a fast screening of promising oxide systems that are prone to exhibit this mechanism in the context of similar solid-state catalytic reaction pathways, potentially reducing the required hydrogen partial pressure and the overall cost of such one-step metallurgical processes.

Conclusion

In summary, we have demonstrated a two-fold kinetic enhancement in the single-step hydrogen co-reduction of Fe_2O_3 with NiO, yielding Fe–Ni alloys via a previously unexplored solid–solid catalytic pathway. Reduction of NiO produces Ni-rich fcc domains that (1) catalyse $Fe_{1-x}O$ reduction through H_2 spillover at dynamically reorganizing metal–oxide interfaces; (2) undergo redox-driven partitioning into Fe oxides, regenerating active interfaces; and (3) directly alloy with reduced Fe at accelerated diffusion rates, bypassing the nucleation process of bcc Fe. These coupled effects enable rapid fcc Fe–Ni alloy formation at 700 °C, lowering energy use and CO_2 emissions while reducing reliance on carbon-intensive routes. The

findings constitute mechanistic foundations that can leverage an appreciable leap towards more sustainable metallurgical extraction methods.

Methods

Material preparations

Fe_2O_3 (VWR Chemicals, 325 mesh, <44 µm, ≥99.7% purity) and NiO powders (Merck kGaA, 325 mesh, <44 µm, ≥99.7% purity) were selected as starting materials, and Ni powders (Nangong Yingtai Metal Materials, 200–300 nm, ≥99.9% purity) were used for comparison. The powders were proportioned to match the Fe–Ni composition of conventional Fe–36 wt.% Ni Invar alloy (equivalent to Fe–34.8 at.% Ni), with a total target mass of 10 g, and thoroughly homogenized in an agate mortar and pestle. For kinetic studies of the catalytic effect, 50 mg of the mixed powders was used to eliminate any sample size effect. For bulk reduction experiments, 0.2 g of the mixtures was pressed into cylindrical pellets (~13 mm in diameter and 2 mm in thickness) using a hydraulic press at a load of ~3.75 t. For subsequent 4D-STEM and APT analyses, site-specific specimens were prepared using a plasma-focused ion beam (PFIB, FEI Helios) equipped with an Xe-ion source. A final low-energy cleaning step (5-keV, 10-pA plasma beam) was applied to minimize ion implantation and surface amorphization due to its limited penetration depth.

Thermogravimetric analysis

Reduction behaviour was studied using a thermogravimetric analyser (TA instrument, DynTHERM-TGA)[5]. To examine the catalytic effect on the reduction kinetics and to eliminate any sample size effects, mixed powders (50 mg) were first heated in argon (Air Liquide, 99.999% purity) at 20 °C min^{-1} to 700 °C, then exposed to hydrogen (10 l h^{-1}, Air Liquide, 99.999% purity) under isothermal conditions for 30 min, followed by cooling to room temperature in argon. For bulk reduction, the powders were compacted into pellets with diameter of ~6.35 mm and thickness of ~2 mm. Continuous heating reduction experiments were conducted using these compacted pellets, heated in hydrogen (10 l h^{-1}, Air Liquide, 99.999% purity) at 5 °C min^{-1} to 700 °C, followed by an isothermal hold stage in hydrogen (10 l h^{-1}, Air Liquide, 99.999% purity) for 2 h before cooling. Instantaneous mass loss was continuously monitored, and conversion fractions were calculated by dividing the observed weight loss by the theoretical weight loss expected for complete Fe_2O_3 → Fe and NiO → Ni reduction. Intermediate states were obtained by interrupting the measurement with high-flow argon.

In situ SXRD study

In situ synchrotron X-ray experiments were performed at beamline P02.1 of PETRA III (DESY), utilizing a high-energy X-ray beam with a wavelength of 0.20735 Å. A working distance of 1,700 mm was selected to achieve an optimal balance between angular resolution and the number of observable Debye–Scherrer rings; this was precisely calibrated using standard LaB_6 powders standardized by NIST. For measurements, pre-compacted Fe_2O_3 and NiO powders were sealed inside a fused-silica capillary tube (inner diameter of ~0.6 mm), with a standard type-K thermocouple positioned adjacent to the sample for accurate temperature monitoring. Heating was achieved via a hot air blower integrated with a PID (proportional–integral–derivative) controller. Additional calibration was performed to correct for discrepancies between the set temperature of the blower and the actual sample temperature. A moderate temperature of 700 °C was chosen for the process to showcase the kinetic significance at only ~0.55 times the T_m of bulk Fe or Ni. High-purity H_2 (purity 99.999%, 1 atm) was introduced through the capillary during heating at a moderate flow rate of ~0.6 l h^{-1} to reduce convection-induced cooling. The flow rate was chosen to achieve sufficient gas exchange throughout the measurement, thereby preventing any kinetic artefacts that might arise from a lack of gaseous reductant.

Two-dimensional diffraction patterns were recorded every 2 s with a beam size of 500 × 500 $µm^2$ to capture the onset of reduction and phase evolution. Data processing was carried out using the open-source software GSAS-II[55]. Azimuthal integration was limited to one quadrant (0–90°) of each Debye–Scherrer ring, and peak shifts were evaluated using a Gaussian–Lorentzian fitting algorithm[56]. Quantitative phase analysis was conducted through Rietveld refinement, ensuring that each fit achieved a weighted-profile R-factor (R_{wp}) below 10%.

4D-STEM characterization

We used 4D-STEM to analyse the crystallographic orientations and phase distributions within the reaction products. The initial 4D-STEM measurements were conducted using a JEM-2200FS microscope (JEOL) operated at an accelerating voltage of 200 kV. This instrument was equipped with a NanoMEGAS precession electron diffraction (PED) system, operated at a frequency of 100 Hz with a precession half-angle of 0.1°, allowing for enhanced orientation precision and reduction of dynamical diffraction effects.

Complementary 4D-STEM data were acquired using a Tescan TENSOR STEM instrument at the Ernst Ruska Centre (ER-C), Forschungszentrum Jülich. This system was operated at 100 kV and used a higher precession angle of 0.5° to improve the reliability of phase and orientation mapping in fine-grained regions. A fast pixelated STEM detector enabled the collection of full diffraction patterns at each probe position across the scanned area.

The data were processed using the commercial ASTAR/ACOM software suite (NanoMEGAS), which performs template matching of experimental diffraction patterns and simulated patterns to generate orientation and phase maps. Virtual bright-field (VBF) and virtual dark-field (VDF) images were reconstructed from the 4D-STEM dataset to enhance contrast and facilitate interpretation. The resulting crystallographic maps revealed the spatial arrangement of fcc grains, residual $Fe_{1-x}O$ regions, grain boundaries and twin boundaries.

Correlative atom probe tomography

Following the acquisition of 4D-STEM data, we performed APT analysis on exactly the same needle-shaped specimen to enable fully correlative structural and compositional analysis at the atomic scale. The APT measurements were carried out using a LEAP 5000XR instrument (CAMECA Instruments), operated at a specimen temperature of 90 K. Laser pulsing conditions were set to a pulse energy of 100 pJ and a pulse rate of 200 kHz, with an average detection rate of 1%. Data processing and 3D reconstruction were performed using the AP Suite 6.3 software (CAMECA), with the image compression factor and k-factor determined through iterative alignment with the STEM image of the specimen to achieve accurate spatial fidelity. To quantify elemental distributions across interfaces, 1D composition profiles were extracted using a cylindrical region of interest with a diameter of 20 nm and a sampling step of 0.5 nm.

DFT-based simulations

Atomistic simulations were performed within DFT, as implemented in the VASP code[57]. Projector-augmented wave pseudopotentials were used to model Fe, Ni and O atoms, containing 8, 10 and 6 valence electrons, respectively. The Brillouin zone was sampled using a grid with a smallest spacing of 0.15 $Å^{-1}$ between k points. For this analysis, we performed DFT calculations considering two different exchange and correlation (x-c) functionals, namely the generalized gradient approximation Perdew–Burke–Ernzerhof (GGA-PBE) and metaGGA-r^{2}SCAN. Although GGA functionals underestimate the thermodynamic properties of transition-metal oxides, such as their formation enthalpies, the later metaGGA-r^{2}SCAN x-c functional yields a much better agreement with experimental references[58,59] while remaining a semi-local method, thus motivating its use in the present analysis. For these reasons, we expect that the DFT results obtained with the metaGGA x-c functional to be more robust and accurate for rationalization of the thermodynamic driving force behind the observed solid-state partitioning and thus focused on these results for further analysis. The results according to both DFT x-c functionals are presented in

detail in Supplementary Tables 1 and 2. We used the two GGA-PBE and metaGGA-r^{2}SCAN[58] exchange and correlation functionals in all presented calculations.

All DFT calculations were spin-polarized in the collinear approximation, as all considered materials have an ordered magnetic ground state, namely ferromagnetic for both bcc Fe and fcc Ni, antiferromagnetic along the <111> directions for FeO and NiO, ferrimagnetic for Fe_3O_4 and antiferromagnetic along the [0001] direction for Fe_2O_3.

All bulk prototypes were fully relaxed until all components of the remaining forces acting on atoms and stresses on the simulation cells fell below 5 meV Å^{-1} and 5 meV Å^{-2}, respectively. The bulk partitioning enthalpy H_P between two materials containing A and B metal species, respectively, is defined as

$$H_P = [E(A^{+B}) + E(B^{+A})] - [E(A) + E(B)]$$

where $E(A^{+B})$ and $E(B^{+A})$ are the DFT total energies of a simulation cell containing bulk A with one substitutional B atom, and bulk B with one A atom, respectively, and $E(A)$ and $E(B)$ are the total energies of the two pristine bulk materials.

The structural models used to model the two configurations of the fcc Ni/FeO interface, the $\{111\}_{Fe}$- and $\{111\}_{O}$-terminated structures presented in Fig. 5b, respectively, contain seven layers of Ni and nine layers of FeO, and eight layers of Ni and 11 layers of FeO in the [111] directions. Both the fcc Ni and FeO slabs are equally strained to accommodate the lattice mismatch between the two materials. The equilibrium position of the two fcc Ni and FeO slabs with respect to each other is then determined, before the interface is fully relaxed with respect to the direction perpendicular to the interface plane and the positions of the atoms. The partitioning enthalpy at the interface is then evaluated by swapping one Ni atom of the fcc slab with one Fe atom from the FeO slab, both coming from the atomic plane closest to the interface.

Data availability

The data supporting the findings of the study are available within the paper and its Supplementary Information.

References

1. Hiorns, A. H. *Principles of Metallurgy* (Macmillan, 1914).
2. Raabe, D., Tasan, C. C. & Olivetti, E. A. Strategies for improving the sustainability of structural metals. *Nature* **575**, 64–74 (2019).
3. Harvey, J.-P. et al. Greener reactants, renewable energies and environmental impact mitigation strategies in pyrometallurgical processes: a review. *MRS Energy Sustain.* **9**, 212–247 (2022).
4. Watari, T., Hata, S., Nakajima, K. & Nansai, K. Limited quantity and quality of steel supply in a zero-emission future. *Nat. Sustain.* **6**, 336–343 (2023).
5. Wei, S. L., Ma, Y. & Raabe, D. One step from oxides to sustainable bulk alloy. *Nature* **633**, 816–822 (2024).
6. van Deelen, T. W., Hernández Mejía, C. & de Jong, K. P. Control of metal-support interactions in heterogeneous catalysts to enhance activity and selectivity. *Nat. Catal.* **2**, 955–970 (2019).
7. Turkdogan, E. & Vinters, J. Gaseous reduction of iron oxides: Part I. Reduction of hematite in hydrogen. *Metall. Mater. Trans. B* **2**, 3175–3188 (1971).
8. Wang, R. R., Zhao, Y. Q., Babich, A., Senk, D. & Fan, X. Y. Hydrogen direct reduction (H-DR) in steel industry—an overview of challenges and opportunities. *J. Clean. Prod.* **329**, 129797 (2021).
9. Spreitzer, D. & Schenk, J. Reduction of iron oxides with hydrogen—a review. *Steel Res. Int.* **90**, 1900108 (2019).
10. Raabe, D. The materials science behind sustainable metals and alloys. *Chem. Rev.* **123**, 2436–2608 (2023).
11. Meyers, M. A. & Tantevee, T. Stresses induced in iron-ore pellets by hydrogen reduction. *Metall. Trans. B* **17**, 217–227 (1986).
12. Turkdogan, E. T., Olsson, R. G. & Vinters, J. V. Gaseous reduction of iron oxides: Part II. Pore characteristics of iron reduced from hematite in hydrogen. *Metall. Trans.* **2**, 3189–3196 (1971).
13. El-Geassy, A. A. & Nasr, M. I. Influence of the original structure on the kinetics of hydrogen reduction of hematite compacts. *Trans. Iron Steel Inst. Jpn* **28**, 650–658 (1988).
14. Cavaliere, P., Perrone, A., Marsano, D. & Primavera, V. Hydrogen-based direct reduction of iron oxides pellets modeling. *Steel Res. Int.* **94**, 2200791 (2023).
15. Avrami, M. Kinetics of phase change. I General theory. *J. Chem. Phys.* **7**, 1103–1112 (1939).
16. Bai, Y. et al. Chemo-mechanical phase-field modeling of iron oxide reduction with hydrogen. *Acta Mater.* **231**, 117899 (2022).
17. Zhou, X. et al. Complexions at the iron-magnetite interface. *Nat. Commun.* **16**, 2705 (2025).
18. Pozzo, M. & Alfe, D. Hydrogen dissociation and diffusion on transition metal (=Ti, Zr, V, Fe, Ru, Co, Rh, Ni, Pd, Cu, Ag)-doped Mg(0001) surfaces. *Int. J. Hydrogen Energy* **34**, 1922–1930 (2009).
19. Conway, B. & Bockris, J. O. M. The *d*-band character of metals and the rate and mechanism of the electrolytic hydrogen evolution reaction. *Nature* **178**, 488–489 (1956).
20. Nørskov, J. K. et al. Trends in the exchange current for hydrogen evolution. *J. Electrochem. Soc.* **152**, J23 (2005).
21. Skúlason, E. et al. Modeling the electrochemical hydrogen oxidation and evolution reactions on the basis of density functional theory calculations. *J. Phys. Chem. C* **114**, 18182–18197 (2010).
22. Jaramillo, T. F. et al. Identification of active edge sites for electrochemical H_2 evolution from MoS_2 nanocatalysts. *Science* **317**, 100–102 (2007).
23. Hu, S. & Li, W.-X. Sabatier principle of metal-support interaction for design of ultrastable metal nanocatalysts. *Science* **374**, 1360–1365 (2021).
24. Minaev, E. & Mryakina, T. Alloyed powders produced by reduction of a complex oxide. *Sov. Powder Metall. Met. Ceram.* **7**, 83–85 (1968).
25. de Alvarenga Oliveira, V., de Jesus Taveira Lana, R., da Silva Coelho, H. C., Brigolini, G. J. S. & dos Santos, C. G. Kinetic studies of the reduction of limonitic nickel ore by hydrogen. *Metall. Mater. Trans. B* **51**, 1418–1431 (2020).
26. Liu, X., Fu, Q. & Shen, X. Theoretical study of hydrogen desorption on the Ni(100) surface through simulated temperature programmed desorption spectra. *Surf. Sci.* **744**, 122467 (2024).
27. van Helden, P., van den Berg, J.-A. & Weststrate, C. J. Hydrogen adsorption on Co surfaces: a density functional theory and temperature programmed desorption study. *ACS Catal.* **2**, 1097–1107 (2012).
28. Sermon, P. & Bond, G. Hydrogen spillover. *Catal. Rev.* **8**, 211–239 (1974).
29. Wang, T. et al. Nature of metal-support interaction for metal catalysts on oxide supports. *Science* **386**, 915–920 (2024).
30. Parravano, G. The reduction of nickel oxide by hydrogen. *J. Am. Chem. Soc.* **74**, 1194–1198 (1952).
31. Zaera, F. The long and winding road to catalysis. *Nature* **541**, 37–38 (2017).
32. Shen, H., Li, H., Yang, Z. & Li, C. Magic of hydrogen spillover: understanding and application. *Green Energy Environ.* **7**, 1161–1198 (2022).
33. Pan, Y. et al. Alloying effects on iron oxide redox pathways: insights into sustainable hydrogen-based reduction. *J. Phys. Chem. Lett.* **16**, 5506–5514 (2025).
34. Sastri, M. V. C., Viswanath, R. P. & Viswanathan, B. Studies on the reduction of iron oxide with hydrogen. *Int. J. Hydrogen Energy* **7**, 951–955 (1982).
35. Zhou, X. et al. Effect of pore formation on redox-driven phase transformation. *Phys. Rev. Lett.* **130**, 168001 (2023).

36. He, K., Zheng, Z. & Chen, Z. A numerical investigation on the hydrogen reduction of wüstite using a 2D mesoscale method. *Int. J. Hydrogen Energy* **47**, 8118–8129 (2022).
37. Moujahid, S. E. & Rist, A. The nucleation of iron on dense wustite: a morphological study. *Metall. Trans. B* **19**, 787–802 (1988).
38. Kim, S.-H. et al. Influence of microstructure and atomic-scale chemistry on the direct reduction of iron ore with hydrogen at 700 °C. *Acta Mater.* **212**, 116933 (2021).
39. Meng, Q., Rong, Y. & Hsu, T. Y. Nucleation barrier for phase transformations in nanosized crystals. *Phys. Rev. B* **65**, 174118 (2002).
40. Dalvi, A. & Smeltzer, W. A diffusion model for oxidation of nickel-iron alloys at 1,000 °C. *J. Electrochem. Soc.* **121**, 386 (1974).
41. Shewmon, P. *Diffusion in Solids* (Springer, 1989).
42. Fukai, Y., Shizuku, Y. & Kurokawa, Y. Superabundant vacancy formation in Ni-H alloys. *J. Alloy Compd* **329**, 195–201 (2001).
43. Du, J.-P., Geng, W., Arakawa, K., Li, J. & Ogata, S. Hydrogen-enhanced vacancy diffusion in metals. *J. Phys. Chem. Lett.* **11**, 7015–7020 (2020).
44. Kim, S.-H. et al. Understanding atom probe's analytical performance for iron oxides using correlation histograms and ab initio calculations. *New J. Phys.* **26**, 033021 (2024).
45. Chen, M. S. & Goodman, D. W. The structure of catalytically active gold on titania. *Science* **306**, 252–255 (2004).
46. Tang, H. et al. Classical strong metal-support interactions between gold nanoparticles and titanium dioxide. *Sci. Adv.* **3**, e1700231 (2017).
47. Cargnello, M. et al. Control of metal nanocrystal size reveals metal-support interface role for ceria catalysts. *Science* **341**, 771–773 (2013).
48. Rousseau, R., Glezakou, V.-A. & Selloni, A. Theoretical insights into the surface physics and chemistry of redox-active oxides. *Nat. Rev. Mater.* **5**, 460–475 (2020).
49. Somorjai, G. A. & Li, Y. *Introduction to Surface Chemistry And Catalysis* Vol. 2 (Wiley, 1994).
50. Ruiz Puigdollers, A., Schlexer, P., Tosoni, S. & Pacchioni, G. Increasing oxide reducibility: the role of metal/oxide interfaces in the formation of oxygen vacancies. *ACS Catal.* **7**, 6493–6513 (2017).
51. Kröger, F. & Vink, H. in *Solid State Physics* (eds Seitz, F. & Turnbull, D.) Vol. 3, p. 307 (Academic Press, 1956).
52. Radler, M. J., Cohen, J. B. & Faber, J. Point defect clusters in wüstite. *J. Phys. Chem. Solids* **51**, 217–228 (1990).
53. Wulf, G. L., Carter, T. J. & Wallwork, G. R. The oxidation of FeNi alloys. *Corros. Sci.* **9**, 689–701 (1969).
54. Channing, D., Graham, M. & Swallow, G. A Mössbauer study of the oxidation of Fe-Ni alloys at 535 and 635 °C. *J. Mater. Sci.* **12**, 2475–2487 (1977).
55. Toby, B. H. & Von Dreele, R. B. GSAS-II: the genesis of a modern open-source all purpose crystallography software package. *Appl. Crystallogr.* **46**, 544–549 (2013).
56. Wei, S. L., Kang, J. & Tasan, C. C. An in situ synchrotron X-ray study of reverse austenitic transformation in a metastable FeMnCo alloy. *J. Mater. Res.* **38**, 281–296 (2023).
57. Kresse, G. & Furthmüller, J. Efficiency of ab-initio total energy calculations for metals and semiconductors using a plane-wave basis set. *Comput. Mater. Sci.* **6**, 15–50 (1996).
58. Kothakonda, M. et al. Testing the r^2SCAN density functional for the thermodynamic stability of solids with and without a van der Waals correction. *ACS Mater. Au* **3**, 102–111 (2022).
59. Swathilakshmi, S., Devi, R. & Sai Gautam, G. Performance of the r^2SCAN functional in transition metal oxides. *J. Chem. Theory Comput.* **19**, 4202–4215 (2023).

Acknowledgements

X.C. and B.G. acknowledge support from the Collaborative Research Centre/Transregio (CRC/TRR) 270 HoMMage-Z01 project funded by the Deutsche Forschungsgemeinschaft (DFG). S.L.W. acknowledges financial support from Alexander von Humboldt Research Fellowship (hosted by D.R.). D.R. is grateful for financial support through the ERC Advanced Grant ROC (grant agreement no. 101054368). D.R. and S.L.W. acknowledge support from an MPG-FhG Cooperation Grant MaRS. X.Z. acknowledges support from the National Natural Science Fund for Excellent Young Scientists Fund Program (Overseas). T.Y. acknowledges support from the Research Infrastructure Access in Nanoscience & Nanotechnology (RIANA) project, funded by the European Union (101130652). SXRD measurements were carried out at beamlines P02.1 and P21.1 at PETRA III of the Deutsches Elektronen-Synchrotron (DESY, proposals I-20231121, I-20240759, I-20240761 and I-20240761). We thank U. Tezins and A. Sturm for their support at the FIB and APT facilities at MPI Sus-mat. We are also grateful to A. Kwiatkowski da Silva for insightful discussion on thermodynamics.

Author contributions

S.W., X.Z. and D.R. conceived the idea and supervised the research. X.C., S.L.W. and T.Y. performed the experiments and analysed all the data. B.G. assisted with the atom probe data analysis. X.Z. assisted with electron microscopy data analysis. B.B. performed the atomistic simulations. X.C., S.L.W., X.Z. and D.R. rationalized all the results. X.C., B.B. and D.R. wrote the original draft of the paper. D.R. acquired the major funding for the research. All authors discussed and approved the final version of the paper.

Funding

Open access funding provided by Max Planck Society.

Competing interests

The authors declare no competing interests.

Additional information

Supplementary information The online version contains supplementary material available at https://doi.org/10.1038/s44160-026-01086-5.

Correspondence and requests for materials should be addressed to Shaolou Wei, Xuyang Zhou or Dierk Raabe.

Peer review information *Nature Synthesis* thanks Diran Apelian and the other, anonymous, reviewer(s) for their contribution to the peer review of this work. Peer reviewer reports are available. Primary Handling Editor: Eric Piechota, in collaboration with the *Nature Synthesis* team.